A 4He vector zero-field optically pumped magnetometer operated in the Earth-field

François Bertrand, Thomas Jager, Axel Boness, William Fourcault, Gwenael Le Gal, Agustin Palacios Laloy, Jérôme Paulet, Jean-Michel Leger

A ^{4}He vector zero-field optically pumped magnetometer operated in the Earth-field

Cite as: XXXXXXXXXX
Submitted: XXXXXXX
Published online: XXXXXXXX

F. Bertrand[1], T. Jager[1,*], A. Boness[1], W. Fourcault[1], G. Le Gal[1], A. Palacios-Laloy[1], J. Paulet[1] and J.-M. Léger[1]

[1]Univ. Grenoble Alpes, CEA, Leti, F-38000 Grenoble, France
*Corresponding author: thomas.jager@cea.fr

ABSTRACT

Low intrinsic noise, high bandwidth and high accuracy vector magnetometers are key components for many ground or space geophysical applications. Here we report the design and the test of a ^{4}He vector optically pumped magnetometer specifically dedicated to these needs. It is based on a parametric resonance magnetometer architecture operated in the Earth magnetic field with closed-loop compensation of the 3 components of the magnetic field. It provides offset-free vector measurements in a ±70 µT range with a DC to 1 kHz bandwidth. We demonstrate a vector sensitivity up to 130 fT/√Hz, which is about ten times better than the best available fluxgate magnetometers currently available for the same targeted applications.

I. INTRODUCTION

High precision and high bandwidth vector magnetic measurements in the Earth field range are usually performed with fluxgate magnetometers [1–3]. However, this technology has an intrinsic sensitivity limited to a few pT/√Hz due to the Barkhausen noise [4,5]. Moreover, fluxgate magnetometers exhibit offsets in the range of several nT that affect their accuracy, thus requiring periodic or continuous calibration with additional high accuracy scalar measurements provided by atomic scalar magnetometers [3,6,7], and among them Optically Pumped Magnetometers (OPM).

There are ways to operate scalar OPM in a vector mode using slow modulation fields [8] which have been tested with success [9], but vector measurements are provided with degraded bandwidth and sensitivity w.r.t. the scalar ones.

The two kinds of magnetometers which deliver better vector sensitivities, below 100 fT/√Hz, and large bandwidths, are usually operated in nearly zero field (i.e. lower than a fraction of a µT) magnetic environment. The first one is the Superconducting QUantum Interference Device (SQUID) [10], which however requires cryogenic cooling. The second one is the zero-field OPM, either based of Hanle effect or parametric resonance, which can reach similar sensitivities without cooling [11].

This advantage has led the development of zero-field OPM for biomagnetic imaging applications such as MagnetoCardioGraphy (MCG) [12–15] or MagnetoEncephaloGraphy (MEG) [16–20]. Most of these sensors rely on alkali operating in the SERF regime and have dynamic ranges of a few nT. Even if compensation of the magnetic field can improve this figure [18,21,22] the dynamic range is far from reaching the Earth field. Thus MCG and MEG recordings out of shieldings have been performed with scalar magnetometers [23,24], but scalar data is poorer than vector data [25,26]. The successful operation of a magnetometer based on the SERF effect in Earth field has been reported [27], but the breakdown of the SERF regime due to high-amplitude noises led to a degraded performance of 1 pT/√Hz.

In this paper we describe the development and the test of a ^{4}He vector OPM which can be operated in the Earth magnetic field. It is based on null-field magnetometers made in our laboratory since early 2000's for space applications, and later adapted for medical imaging applications (Section II, [10,11]). It is complemented with a with a real-time compensation of the field thanks to a compact tri-axial coil and a dedicated

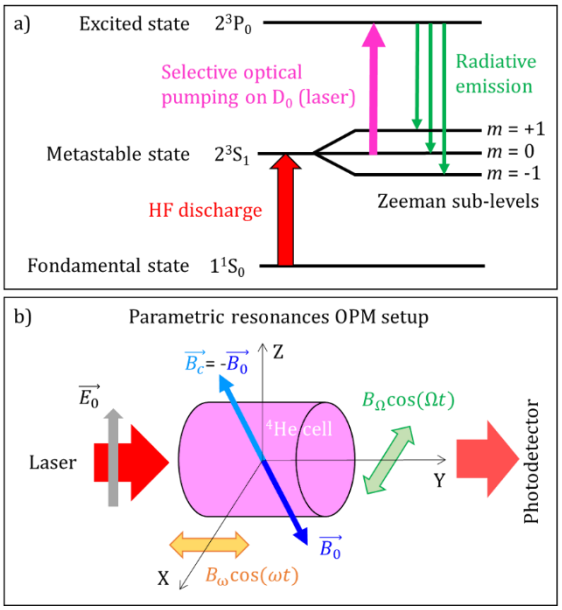

FIG. 1. (a) Simplified principle of operation of the ^{4}He OPM: energy diagram describing the optical pumping process (b) and main elements of the parametric resonance magnetometer architecture.

electronics (Section III). This sensor meets the ±70 µT range requirement, allows offset-free vector measurements with an intrinsic noise very similar to the one obtained in zero-field, and its bandwidth exceeds 1 kHz (Section IV).

II. PHYSICAL PRINCIPLE

The physical principle used for the operation of our OPM (FIG. 1) is described in [28].

It is based on the parametric resonances of ^{4}He metastable atoms in a near zero magnetic field [29].

In this sensor the sensitive element is a gas of ^{4}He atoms in their 2^3S_1 metastable state. This state is first populated with a high frequency (HF) discharge that brings ^{4}He atoms from the ground state to the metastable state. Then a alignment polarization is created by optically pumping the metastable state using the D_0 ($2^3S_1 \rightarrow 2^3P_0$, $F=1 \rightarrow F'=0$) transition at 1083.2 nm wavelength with linearly polarized light (polarization $\overrightarrow{E_0}$ along the Z axis). Two orthogonal oscillating radio-frequency (RF) magnetic fields $B_\Omega cos\Omega t$ and $B_\omega cos\omega t$ are injected respectively along the X and Y axes of the sensor and excite null-field parametric resonances ([30,28]). To the first order, the photodetection signal displays three signals at Ω, ω and $\Omega \pm \omega$ angular frequencies whose amplitudes are proportional to B_X, B_Y and B_Z respectively.

The antisymmetric shape of the in-phase demodulated resonance signals at Ω, ω and $\Omega \pm \omega$ (FWHM typically in the 100 nT range) is then used to operate the magnetometer in a closed-loop configuration: a compensation magnetic field $\overrightarrow{B_c}$ counterbalancing the magnetic field $\overrightarrow{B_0}$ is continuously generated in the vector compensation coils surrounding the ^{4}He gas cell to maintain the null field condition. The measurement of the three components of the magnetic field $\overrightarrow{B_0}$ is obtained from the measurement of the compensation currents. This principle of operation is very similar to the one of a closed-loop fluxgate magnetometer.

III. DESIGN

The architecture of the sensor detailed here directly derives from the ones developed in our laboratory for MEG applications whose detailed description can be found in [21], and the typical noise obtained with this technology is around 50 fT/√Hz for the X and Y axes, and 200 fT/√Hz for the third axis Z.

Operating this MEG-based sensor architecture in the Earth magnetic field raises two additional design constraints in order to achieve similar noise performance.

The first one is the magnetic field gradient generated inside the ^{4}He cell by the compensation magnetic field. This gradient has the effect of broadening the resonance signals that drive the magnetometer servo-loops, degrading its sensitivity. Section III-A reports the design of a tri-axial compensation coil, resulting from the tradeoff between the sensor head size and the noise performance.

The second one concerns the electronics: to keep an intrinsic noise of 50 fT/√Hz over a dynamic range of ±70 µT requires a magnetic field compensation loop with a 180 dB/√Hz normalized Signal to Noise Ratio (SNR). Section III-B presents the architecture and the achieved performances of the electronics designed to meet this requirement.

A. Design of the tri-axial compensation coil

The impact of a magnetic field gradient on the parametric resonance magnetometer was first experimentally characterized thanks to a dedicated test set-up described in FIG. 2.a.

In this test setup, a ^{4}He MEG sensor (FIG. 2.b) is set inside a high homogeneity 3-axial coil to compensate the static Earth magnetic field (FIG. 2.c, magnetic field homogeneity better than 1×10^{-4} over the whole volume of the ^{4}He cell to avoid any signal degradation). Magnetic gradients are then superimposed to the system thanks to a Helmholtz coil operated in an axial gradient configuration (cf FIG. 2.d) and the impact on the parametric resonance signals characteristics is observed successively on each sensor axis.

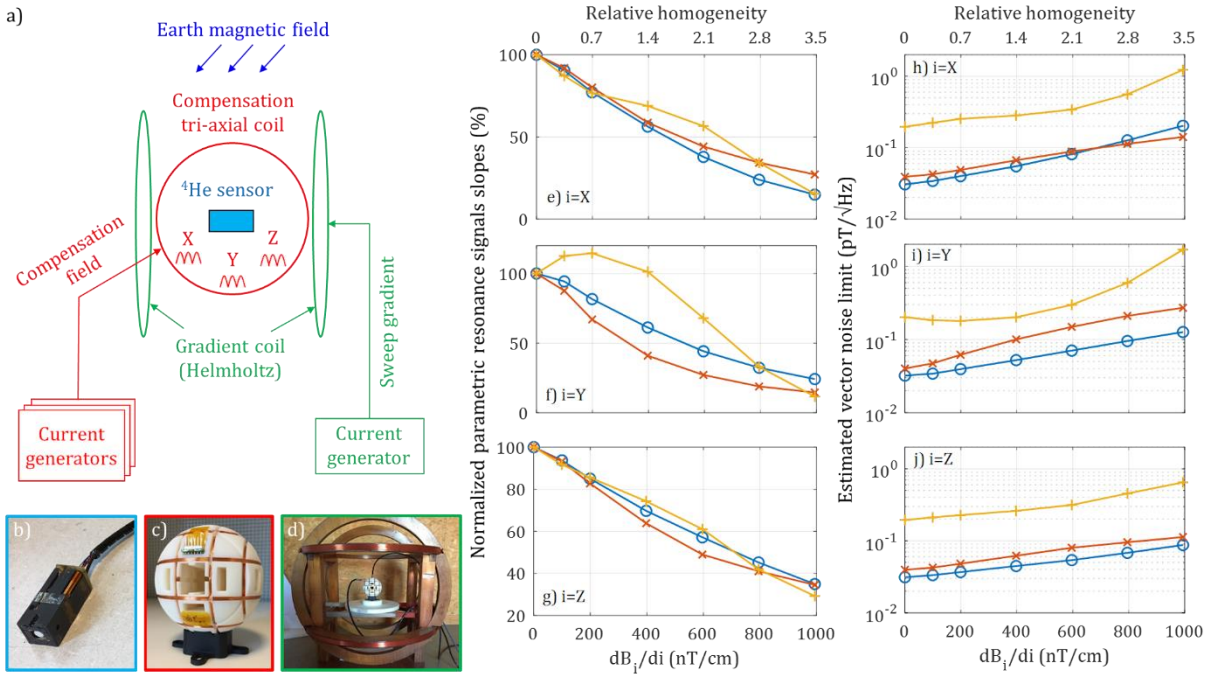

FIG. 2. Impact of magnetic field gradients on the parametric resonance magnetometer. (a) Schematic drawing of the gradient characterization test setup. (b) ^{4}He MEG sensor used for the test. (c) High homogeneity compensation coil, better than 1×10^{-4} over the whole volume of the ^{4}He cell (d) Helmholtz coils used in an axial gradient coil configuration. (e,f,g) Evolution in % of the normalized parametric resonance signals slopes along the X (blue), Y (orange) and Z (yellow) axes in function of the dB_X/dX, dB_Y/dY and dB_Z/dZ, axial gradient. (h,i,j) Estimated noise in pT/√Hz along the X (blue), Y (orange) and Z (yellow) axes in function of the magnetic field gradient applied to the ^{4}He cell. A relative homogeneity scale is also added as an upper axis on all figures (in 1×10^{-3} @ B_0 = 70 µT).

The FIG. 2.e to FIG. 2.g illustrate the measured degradation of the slope of the parametric resonance signals for axial gradients up to 1 µT/cm. The observed degradation is at first order linear with the imposed longitudinal or transverse gradient: in the worst case, a 50 % reduction of the resonance signal slopes is observed on the X, Y and Z axes for gradients of about 500, 300 and 700 nT/cm respectively.

Based on these characterizations, we designed a compact tri-axial compensation coil based on a Helmholtz architecture with an outer maximum diameter of 5 cm, which provides a magnetic field homogeneity better than 2×10^{-3} over ^{4}He gas cell. With this coil geometry, the maximum magnetic field gradient generated over the gas cell is about 600 nT/cm @ 70 µT in the most unfavorable compensation configuration. In the worst case, the resulting slopes on the X, Y and Z axes would be respectively reduced by a factor 2.6, 3.3 and 1.8 which would correspond to intrisic noise of 130, 170 and 360 fT/√Hz for the ^{4}He OPM sensor once operated (cf FIG. 2.h to FIG. 2.j). For an operation in our local magnetic field of 47 µT in Grenoble, we expect smaller degradations since the compensation fields are smaller. The noise and the attenuation of the slopes of the resonance signals would be reduced by a factor of 1.5 w.r.t. the 70 µT case.

B. Design of the electronics

The required dynamic range of ±70 µT is by far much larger than the FWHM of the parametric resonances, so that a closed-loop mode operation of the sensor is mandatory [21]. This mode also provides better linearity characteristics to the OPM instrument, where open-loop cross-axis effects are also avoided. The FIG. 3 details such a loop. In our architecture, the signal processing is digital: photodetected signals are first converted thanks to an Analog to Digital Converter (ADC) at the output of the photodetector, parametric resonance signals are then obtained from demodulation and filtering blocks before being processed by integrators blocks. In this architecture, one can extract the measurement of the vector

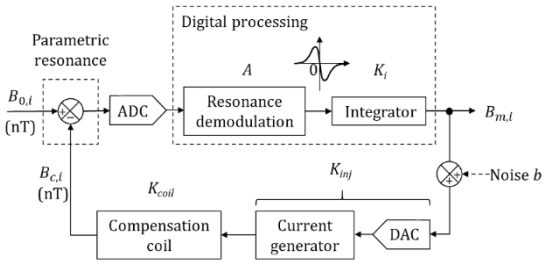

FIG. 3. Schematic of the null-field closed-loop implemented in our electronics for the compensation of the ambient vector magnetic field. In this loop, b models all types of noise sources introduced by the feedback elements as an equivalent input noise.

magnetic field directly at the output of the integrator. The feedback chain is then composed for each axis of a Digital to Analog Converter (DAC), followed by a current generator and the compensation coil. The noise b represented in the FIG. 3 models any noise introduced by the feedback elements as an equivalent input noise.

In this closed-loop operation scheme, the measured output vector magnetic field $B_{m,i}$ ($i \in \{X, Y, Z\}$) can be written as :

$$B_{m,i} = \frac{1}{K_{coil}K_{inj}}\left[\frac{1}{1+\frac{s}{AK_iK_{inj}K_{coil}}}B_{0,i} - \frac{K_{inj}K_{coil}}{1-\frac{s}{AK_iK_{inj}K_{coil}}}b\right] \quad \text{Eq. 1}$$

with s the Laplace variable, K_{coil} the gain of the compensation coil, K_{inj} the injection gain including both the gain of the current generator and the gain of the DAC conversion, K_i the gain of the integrator, and A the gain of the demodulated signals. In Eq. 1, $B_{o,i}$ represents the i^{th} ($i \in \{X, Y, Z\}$) component of the magnetic field $\overrightarrow{B_0}$.

If we neglect the low pass filtering effect of the atomic system (cut-off frequency around 5 kHz), the gain $A(s)$ is constant and the transfer function $B_{m,i}/B_{o,i}$ is a first order low pass filter with static transfer coefficient $(K_{coil}\,K_{inj})^{-1}$ and a time constant $(A\,K_i\,K_{coil}\,K_{inj})^{-1}$.

The Eq. 1 also shows the impact noise on the output $B_{m,i}$ through the feedback chain: it consists in a contribution in the form of a first order low pass filter with the same time constant as the $B_{m,i}/B_{o,i}$ transfer function, with a gain of 1. That means that the noise b is fully transferred to the measurement of the magnetic field $B_{m,i}$.

As mentioned in the introduction of section III, the dynamic range of the electronics is the key point to enable the operation of null-field vector magnetometer in the Earth magnetic field without degradation of its intrinsic noise. This requirement is common with high-resolution fluxgate magnetometers, even if it is a bit relaxed as they exhibit higher intrinsic noise. Publications [3], [31–33] address this topic. In [3] for instance, the electronics noise of the ESA Swarm mission Vector Field Magnetometer (VFM) fluxgate magnetometer is mentioned as the dominant source in the sensor overall noise with a 15 pT/√Hz level at 1 Hz while the intrinsic noise of the sensor head is 6.6 pT/√Hz.

Among all the elements constituting the feedback chain of our ^{4}He OPM (compensation coil, current generator and DAC), the DAC is the most critical one w.r.t our high dynamic and low noise requirement. To fulfill it, we have designed a dedicated high SNR, 28 bits, 64 kSPS DAC, associated with a very low noise current generator.

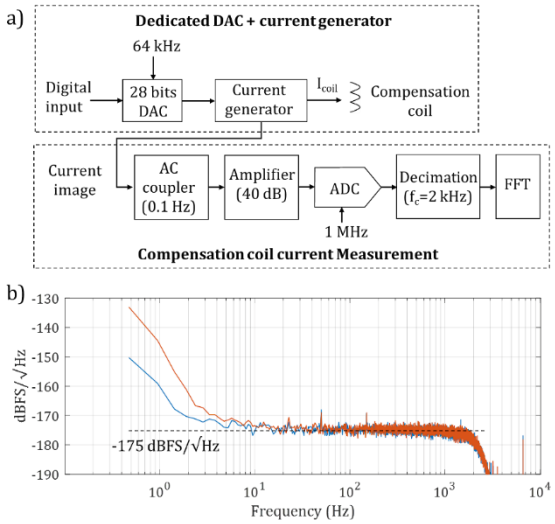

FIG. 4. Noise level performance of the compensation currents delivered by the DAC and current generator assembly in the feedback of the ^{4}He magnetometer closed-loop architecture: characterisation method (a) and noise measurements (b). In (b) the blue spectrum corresponds to a null compensation current, and the orange one to a compensation current close to full scale, i.e. equivalent to a ±70 µT magnetic field compensation.

The performance of the current compensation chain using this DAC is illustrated on the FIG. 4: the characterization method is first described on FIG. 4.a and the noise measurements are given on FIG. 4.b. In this characterization setup of FIG. 4.a, an image of the current injected in the compensation coil from a DC digital input applied to the DAC is acquired through a dedicated acquisition chain composed of an AC coupler (f_c=0.1 Hz), a 40 dB low noise amplifier and a high resolution ADC. The amplification of the acquired signal by the ADC ensures an equivalent input noise of the converter to be much lower than the current noise to characterize. The output digitized signal is then low-pass filtered (f_c=2 kHz) and decimated before performing a power spectral density (FIG. 4.b) displaying the noise characteristics of the injected compensation current.

As shown in FIG. 4.b the measured noise floor is identical for both a null and a full scale compensation, with a measured SNR of 175 dB/√Hz for frequencies higher than a few Hertz. Although it is 5 dB higher than the initial requirement of 180 dB/√Hz, this result can be considered as excellent and translates into an equivalent vector noise of 100 fT/√Hz for a full compensation range of ±70 µT.

We can also notice on the spectra of FIG. 4.b that they both exhibit 1/f-excess noise at low-frequency, but with slightly different magnitudes and slopes: with the null setting input, the noise rise is mainly due to the

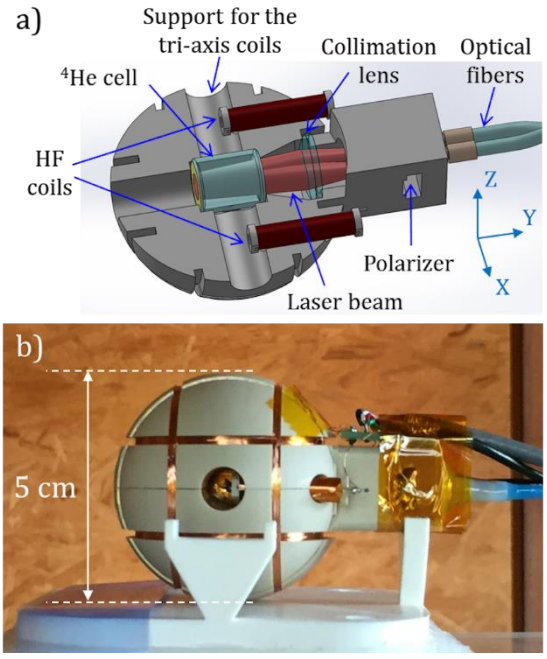

FIG. 5. Drawing (a) and picture (b) of the realized sensor head.

intrinsic noise of the DAC while it is slightly higher for the half full-scale input and mainly due in this case to the noise of the voltage reference used by the DAC.

C. Realized prototype and operational characteristics

The FIG. 5 shows the sensor head architecture of our zero-field ^{4}He OPM for Earth field operation: the ^{4}He cell is set at the center of a PEEK mechanical structure, including two HF coils for the HF discharge. An input optical fiber delivers the pumping light to the sensor head. The beam is linearly polarized and collimated before reaching the cell. The bottom of the glass cell is coated with a dielectric mirror, which reflects the beam back into a multi-mode optical fiber towards the photodetector which is set on the electronics board.

In nominal operation, the ^{4}He in the cell is excited with a HF discharge at 16 MHz absorbing 40 mW of power. The frequency and amplitude of the RF excitation fields are set to 9 kHz and 150 nT_{peak} and 40 kHz and 800 nT_{peak} respectively for the X and Y axes. In order to deliver a laser beam with intensity noise near the shot noise limit, we used a high performance commercial laser from Toptica. The laser is tuned to the D_0 absorption line at 1083.2058 nm (vacuum std) and its output power is set to 800 µW so that optical power received on the photodetector is about 250 µW.

The dedicated electronics includes all the RF excitation stages, the low noise current generators, the back photodetector and all the associated signal processing stages including ADC and DAC components. The digital

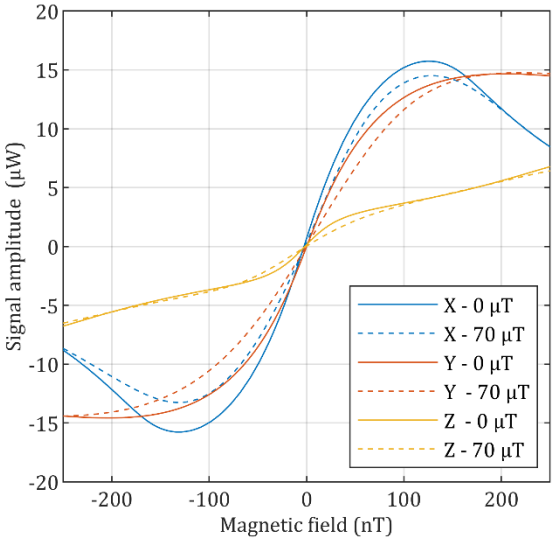

FIG. 6. Parametric resonance signals obtained for each axis of the ^{4}He vector magnetometer (equivalent optical power of the demodulated signal in µW). Signals in null field conditions (continuous curves) and signals obtained in the worst-case magnetic field configurations (70 µT field along each axis, dotted curves). A reduction by 26, 35 and 39 % of the resonance slopes are respectively observed on the X, Y and Z axes between the null field configuration and the full scale 70 µT compensation.

core is based on the Xilinx SoC Zynq 7020 with a Microzed card from the Avnet company.

IV. EXPERIMENTAL RESULTS

The achieved performances of the ^{4}He OPM is presented and reviewed in the following paragraphs. In section IV-A we detail the intrinsic vector noise performance limits derived from the characterization of the parametric resonances signals. The bandwidth of the vector measurements in closed-loop configuration is characterized in section IV-B. In section IV-C, the full ±70 µT vector measurement range in closed-loop operation is demonstrated in a 3D magnetic field generator. In section IV-D, preliminary accuracy figures are derived from the results of a vector calibration performed in Earth magnetic field. The achieved vector noise performance in closed-loop operation is finally detailed in section IV-E.

A. Intrinsic noise performance

The FIG. 6 shows typical parametric resonance signals measured along the X, Y and Z axes of the ^{4}He magnetometer in nominal operation for an null-field magnetic environment and for full scale axial magnetic field compensation configurations (i.e. ±70 µT successively compensated along each of the X, Y and Z axes).

In null field conditions, the slopes corresponding to the X, Y and Z axes are respectively measured about 250 nW/nT, 190 nW/nT and 80 nW/nT (continuous curves

shown on FIG. 6). The photon shot noise corresponding to the received optical power (250 µW) is about 11 pW/√Hz so that the intrinsic vector noise limit of the magnetometer is respectively of about 50 fT/√Hz, 60 fT/√Hz and 140 fT/√Hz on the X, Y and Z axes. In the worst operational cases (i.e. when ±70 µT is compensated along a given axis), the slopes of the resonances signals along the X, Y and Z axes are here respectively reduced by 26, 35 and 39 % (dotted curves of FIG. 6). This is better than expected and this result could be related to the slight differences between both the architecture and the hardware elements of the realized sensor and those of the MEG sensor used for the first characterizations depicted in section III-A.

B. Measurement bandwidth

The bandwidth of the vector measurements in closed-loop configuration was characterized for each axis through the amplitude analysis in the magnetometer measurements of an AC reference signal injected thanks to an external coil system. This characterization was performed in a magnetic shielded environment with a sinusoidal reference signal of fixed amplitude (about 100 pT_{rms}) and a frequency ranging from 0.1 Hz up to 2 kHz. An illustration of the vector measurements performed during this characterization process is given on FIG. 8 for the X axis. A 3 dB attenuation is measured at 1 kHz for each axis, in full agreement with the low-pass filter characteristics of the compensation loop on these axes.

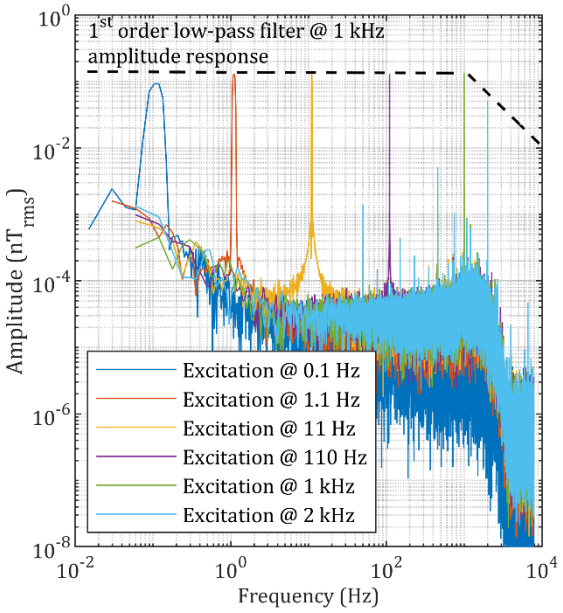

FIG. 8. Bandwidth measurement of the vector OPM operated in closed-loop configuration. Amplitude responses in nT_{rms} measured on the X axis of the magnetometer to external sinusoidal excitation with frequency ranging from 0.1 Hz up to 2 kHz. A [DC-1 kHz] bandwidth is derived from the measurements, in full agreement with the filter characteristics of the closed-loop on this axis.

C. Measurement range

The ±70 µT measurement range verification was carried out inside a magnetic field simulator of the CEA's magnetic test facility at Herbeys (FIG. 7.a and FIG. 7.b), where a magnetic field sweep figure was performed on each axis of the sensor coil frame, as shown in FIG. 7.c and FIG. 7.d.

The FIG. 7.e and FIG. 7.f display the response of the magnetometer during the performed magnetic field ramps and validates the sensor operational vector measurement range of ±70 µT.

D. Vector calibration

The vector calibration method used for the magnetometer is based on the paper from Olsen [7]. It consists first in applying a wide variety of directions of the magnetic field to the ^{4}He magnetometer and then in using an algorithm to minimize the residual between the scalar field (supposed well-known, for instance thanks to an additional measurement delivered by an auxiliary scalar reference magnetometer) and the reconstructed scalar field calculated from the three vector components measured by the sensor. The minimization algorithm provides the 3 vector coil scale factors, 3 orthogonality angles of the coil reference frame, and 3 axis offsets. In refined versions of the algorithm, one can also derive the thermal expansion

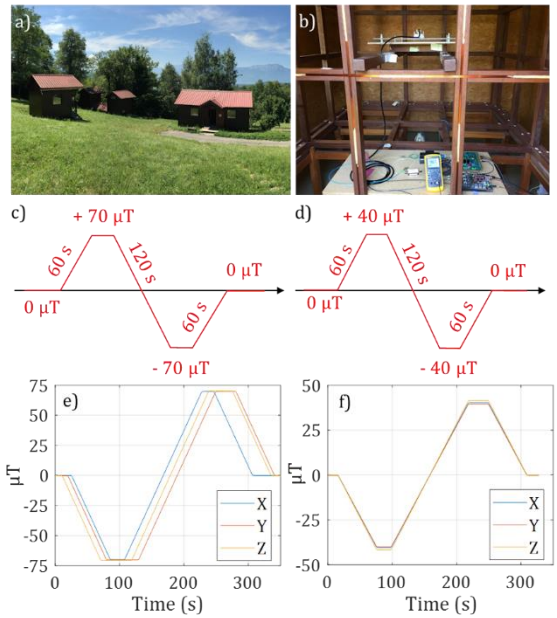

FIG. 7. (a) Non-magnetic cabins of the Herbeys's magnetic test facilities. (b) ^{4}He sensor set inside the field simulator. (c) Field pattern applied to the magnetometer on each axis successively, the magnetic field is set to 0 nT on the others axis. (d) Intercardinal magnetic field applied to the magnetometer. (e) Vector components (µT) measured during the magnetic field sweeps of ±70 µT successively performed on each axis. (f) Vector components (µT) measured during intercardinal magnetic field sweep of ±40 µT (70 µT max total field intensity).

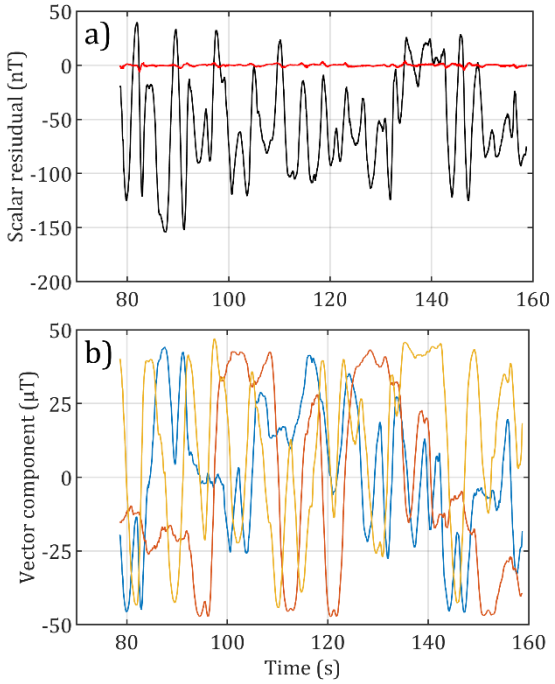

FIG. 9. Vector calibration of the ^{4}He magnetometer. (a) Scalar residual before (black) and after calibration (red). (b) Vector components measured by the ^{4}He OPM during the calibration process: B_X (blue), B_Y (orange) and B_Z (yellow).

characteristics of the compensation coil and cross-axis parameters.

For calibration results presented below, we have calibrated three offsets, three sensitivities, and three non-orthogonality angles.

The FIG. 9 and TABLE 1 show the results of a preliminary vector calibration performed in our magnetic test facilities of Herbeys. This vector calibration was performed through manual orientations of the ^{4}He magnetometer in the local Earth magnetic field of about 47 μT in modulus. The standard deviation of the scalar residual at the output of the calibration process is of 1 nT_{rms}. This preliminary result already confirms both the high linearity of the ^{4}He magnetometer and its ability to address high accuracy applications.

TABLE 1. Vector calibration parameters obtained for the ^{4}He magnetometer.

Parameter	X axis	Y axis	Z axis
Offset (nT)	1.8507	-1.3118	8.9218
Scale factor (nT/V)	10047	10017	9971.1
Orthogonality (°)	0.0582	-0.0144	-0.0387

However, this vector calibration is an early and preliminary demonstration of the vector performances of the ^{4}He OPM as it was characterized with the following limitations:

1. The local magnetic field was considered constant during the acquisition. Its mean value measured with a scalar reference Nuclear Magnetic Resonance (NMR) magnetometer was of 47120 nT during the 80 s of the acquisition. It is likely that it has varied in a range that artificially affected the overall accuracy of the vector field reconstruction (i.e. a few nT peak-to-peak).
2. Even if the local scalar magnetic gradient is very low in our test cabins in Herbeys (< 300 pT/m), small variations between the locations of the NMR reference sensor and the ^{4}He OPM may have occurred during the OPM rotations.

The 1 nT_{rms} figure is thus a current worst case characteristic of the ^{4}He OPM vector field reconstruction, mostly an inherent limitation of this early characterization process that also shows up on the derived offset values. At first order, the larger possible sources of offset are related to the electronics and have been characterized in the nT order of magnitude. The derived values by the calibration algorithm for the X and Y axes are in agreement with these characteristics. An improved vector calibration method is in progress and we expect it to yield new results nearer to the actual precision limits.

E. Closed-loop noise measurements

Noise performances are one of the main improvements of our ^{4}He sensor with respect to state of the art high-accuracy fluxgate magnetometers.

To access the ultimate noise performance of our ^{4}He magnetometer, it has to be isolated from external magnetic field perturbations: the intrinsic noise characterizations were thus conducted inside a Twinleaf MS-2 magnetic shield (4 mu-metal layers shield, cf FIG. 10).

The fluxgate magnetometer chosen for the comparison with our sensor was the Bartington Mag03-MS70 operated with a PSU1 electronic unit. A 24 bits sigma-delta data acquisition system (National Instrument PXIe 4303) operated with a ±100 mV input range was used to acquire the three vector measurements, which ensures an acquisition noise significantly below the sensor's intrinsic noise (100 fT/√Hz for f>10 Hz to be compared to the magnetometer noise of 3 to 4 pT/√Hz).

The FIG. 10.d to FIG. 10.f show the measurements of the vector noise of the two magnetometers. The ^{4}He magnetometer has a noise floor of 130 fT/√Hz on the X

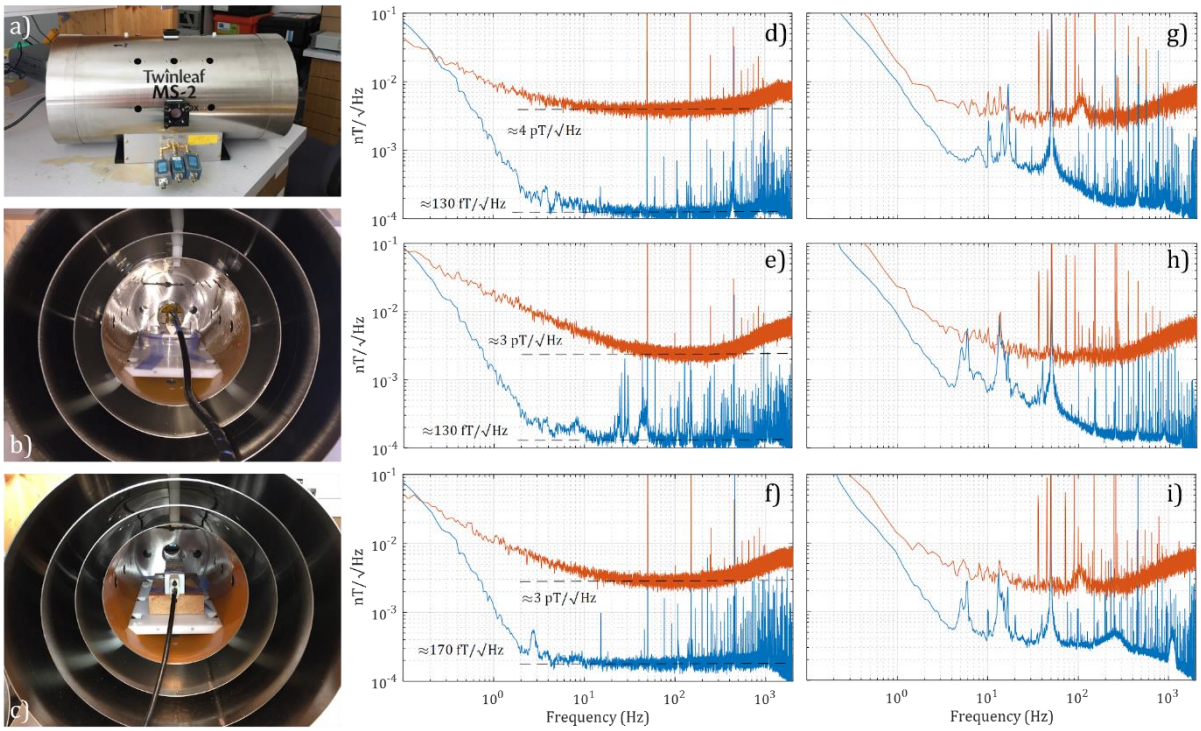

FIG. 10. OPM noise measurements in closed-loop. (a) MS-2 Twinleaf 4 layers magnetic shield. (b) ^{4}He OPM set inside the shield. (c) Mag03-MS70 fluxgate magnetometer set inside the shield. (d,e,f) Noise measurements inside the shield along the X (d), Y (e) and Z (f) axes, OPM measurements in blue, fluxgate measurements in orange. (g,h,i) Noise measurements in ambient Earth magnetic field in Herbeys' facilities along the X (g), Y (h) and Z (i) axes, OPM measurements in blue and fluxgate ones in orange. The local static field in the instruments' reference frames was of B_X = +16 µT, B_Y = -21 µT and B_Z = +42 µT.

and Y axes, and 170 fT/√Hz on the Z axis. This is at least one order of magnitude better than the 3 to 4 pT/√Hz noise floor level of the fluxgate vector measurements.

These measured noise levels are in full agreement with our estimations of the intrinsic vector noise of the sensor and the electronics previously detailed in sections III-A and III-B respectively. Indeed, due to the non-coherence of the magnetic field sources, the total noise of the magnetometer can be estimated by the quadratic sum of these two sources. Thus, for the X and Y axes, the measured noise of 130 fT/√Hz is mainly due to the noise of the electronic (100 fT/√Hz) combined to the intrinsic sensor noise of 50 fT/√Hz and 60 fT/√Hz respectively for the X and Y axes. For the Z axis, the contributions to the overall vector noise are more balanced: the intrinsic noise of the sensor is slightly higher (140 fT/√Hz) than the electronic noise (100 fT/√Hz), leading to a total noise of 170 fT/√Hz, as confirmed by our measurement.

The ^{4}He magnetometer low frequency excess noise is dominated by its electronics as seen in the section III-B: the $1/f$ corner is around 3 Hz in the measured spectrum with a noise of 1 pT/√Hz at 1 Hz. This last characteristics is again well below those of high accuracy fluxgate magnetometers (15 pT/√Hz at 1 Hz for the VFM instrument mentioned in section III-B and similar characteristics for the Bartington Mag03-MS70 fluxgate).

Additional vector noise measurements were also performed in the Earth magnetic field in our Herbeys test facility to probe the ^{4}He magnetometer noise performance in this environment. These measurements are shown on FIG. 10.g to FIG. 10.i, along with those performed with the Bartington Mag03-MS70 high-accuracy fluxgate in the same conditions. These spectra illustrate the various characteristics of the ambient magnetic environment: the low frequency signature of the Earth magnetic field, the local electrical network lines (50 Hz and harmonics), the remaining electronic equipment signatures even if they are not set in the vicinity of the sensor head and electric fences of agricultural fields. Despite these perturbations, we do not observe any degradation of the intrinsic vector noise floor level of the ^{4}He instrument in these measurements. In the end, they highlight once again the very high sensitivity of our ^{4}He vector magnetometer.

V. CONCLUSION

In this paper, we have demonstrated the feasibility to operate a ^{4}He zero-field vector OPM in the Earth magnetic field while keeping good intrinsic noise characteristics. This magnetometer constitutes an advantageous alternative to fluxgates whenever high resolution or high accuracy is required, e.g. for specific geophysical, defense or space applications.

ACKNOWLEDGMENTS

The development of the ^{4}He OPM magnetometer dedicated Earth magnetic field environment has been supported for space applications by CNES ("Centre National d'Etudes Spatiales" i.e. the French space agency) through several R&T actions and for specific on-ground geophysical measurements by BRGM ("Bureau de Recherches Géologiques et Minières", the French geological survey).

DATA AVAILABILITY

The data that support the findings of this study are available from the corresponding authors upon reasonable request.

REFERENCES

[1] F. Primdahl, *The Fluxgate Magnetometer*, J. Phys. [E] **12**, 241 (1979).

[2] P. Ripka, *Review of Fluxgate Sensors*, Sens. Actuators Phys. **33**, 129 (1992).

[3] J. E. M. G. Merayo, J. L. Jorgensen, E. Friis-Christensen, P. Brauer, F. Primdahl, P. S. Jorgensen, T. H. Allin, and T. Denver, *The Swarm Magnetometry Package*, in *Small Satellites for Earth Observation* (2008), pp. 143–151.

[4] H. Bittel, *Noise of Ferromagnetic Materials*, IEEE Trans. Magn. **5**, 359 (1969).

[5] J. L. M. J. Bree, J. A. Poulis, and F. N. Hooge, *Barkhausen Noise in Fluxgate Magnetometers*, Appl. Sci. Res. **29**, 59 (1974).

[6] J. M. G. Merayo, P. Brauer, F. Primdahl, J. R. Petersen, and O. V. Nielsen, *Scalar Calibration of Vector Magnetometers*, Meas. Sci. Technol. **11**, 120 (2000).

[7] N. Olsen, L. Tøffner-Clausen, T. J. Sabaka, P. Brauer, J. M. G. Merayo, J. L. Jørgensen, J. M. Léger, O. V. Nielsen, F. Primdahl, and T. Risbo, *Calibration of the Ørsted Vector Magnetometer*, Earth Planets Space **55**, 11 (2003).

[8] O. Gravrand, A. Khokhlov, J. L. Le Mouël, and J. M. Léger, *On the Calibration of a Vectorial 4He Pumped Magnetometer*, Earth Planets Space **53**, 949 (2001).

[9] G. Hulot, P. Vigneron, J. Léger, I. Fratter, N. Olsen, T. Jager, F. Bertrand, L. Brocco, O. Sirol, X. Lalanne, A. Boness, and V. Cattin, Swarm *'s Absolute Magnetometer Experimental Vector Mode, an Innovative Capability for Space Magnetometry*, Geophys. Res. Lett. **42**, 1352 (2015).

[10] A. Edelstein, *Advances in Magnetometry*, J. Phys. Condens. Matter **19**, 165217 (2007).

[11] I. K. Kominis, T. W. Kornack, J. C. Allred, and M. V. Romalis, *A Subfemtotesla Multichannel Atomic Magnetometer*, Nature **422**, 596 (2003).

[12] S. Morales, M. C. Corsi, W. Fourcault, F. Bertrand, G. Cauffet, C. Gobbo, F. Alcouffe, F. Lenouvel, M. Le Prado, F. Berger, G. Vanzetto, and E. Labyt, *Magnetocardiography Measurements with ^{4} He Vector Optically Pumped Magnetometers at Room Temperature*, Phys. Med. Biol. **62**, 7267 (2017).

[13] A. Weis, G. Bison, N. Castagna, S. Cook, A. Hofer, M. Kasprzak, and P. Knowles, *Mapping the Cardiomagnetic Field with 19 Room Temperature Second-Order Gradiometers*, **28**, 4 (n.d.).

[14] G. Lembke, S. N. Erné, H. Nowak, B. Menhorn, A. Pasquarelli, and G. Bison, *Optical Multichannel Room Temperature Magnetic Field Imaging System for Clinical Application*, Biomed. Opt. Express **5**, 876 (2014).

[15] I. A. Sulai, Z. J. DeLand, M. D. Bulatowicz, C. P. Wahl, R. T. Wakai, and T. G. Walker, *Characterizing Atomic Magnetic Gradiometers for Fetal Magnetocardiography*, Rev. Sci. Instrum. **90**, 085003 (2019).

[16] H. Xia, A. Ben-Amar Baranga, D. Hoffman, and M. V. Romalis, *Magnetoencephalography with an Atomic Magnetometer*, Appl. Phys. Lett. **89**, 211104 (2006).

[17] J. Osborne, J. Orton, O. Alem, and V. Shah, *Fully Integrated Standalone Zero Field Optically Pumped Magnetometer for Biomagnetism*, in *Steep Dispersion Engineering and Opto-Atomic Precision Metrology XI*, Vol. 10548 (International Society for Optics and Photonics, 2018), p. 105481G.

[18] N. V. Nardelli, A. R. Perry, S. P. Krzyzewski, and S. A. Knappe, *A Conformal Array of Microfabricated Optically-Pumped First-Order Gradiometers for Magnetoencephalography*, EPJ Quantum Technol. **7**, (2020).

[19] A. Borna, T. R. Carter, J. D. Goldberg, A. P. Colombo, Y.-Y. Jau, C. Berry, J. McKay, J. Stephen, M. Weisend, and P. D. D. Schwindt, *A 20-Channel Magnetoencephalography System Based on Optically Pumped Magnetometers*, Phys. Med. Biol. **62**, 8909 (2017).

[20] E. Labyt, M.-C. Corsi, W. Fourcault, A. Palacios Laloy, F. Bertrand, F. Lenouvel, G. Cauffet, M. Le Prado, F. Berger, and S. Morales, *Magnetoencephalography With Optically Pumped ^{4} He Magnetometers at Ambient Temperature*, IEEE Trans. Med. Imaging **38**, 90 (2019).

[21] W. Fourcault, R. Romain, G. Le Gal, F. Bertrand, V. Josselin, M. Le Prado, E. Labyt, and A. Palacios-Laloy, *Helium-4 Magnetometers for Room-Temperature Biomedical Imaging: Toward Collective Operation and Photon-Noise Limited Sensitivity*, Opt. Express **29**, 14467 (2021).

[22] R. E. Slocum and F. N. Reilly, *Low Field Helium Magnetometer for Space Applications*, IEEE Trans. Nucl. Sci. **10**, 165 (1963).

[23] M. E. Limes, E. L. Foley, T. W. Kornack, S. Caliga, S. McBride, A. Braun, W. Lee, V. G. Lucivero, and M. V. Romalis, *Portable Magnetometry for Detection of Biomagnetism in Ambient Environments*, Phys. Rev. Appl. **14**, (2020).

[24] R. Zhang, W. Xiao, Y. Ding, Y. Feng, X. Peng, L. Shen, C. Sun, T. Wu, Y. Wu, Y. Yang, Z. Zheng, X. Zhang, J. Chen, and H. Guo, *Recording Brain Activities in Unshielded Earth's Field with*

Optically Pumped Atomic Magnetometers, Sci. Adv. **6**, eaba8792 (2020).

[25] M. J. Brookes, E. Boto, M. Rea, V. Shah, J. Osborne, N. Holmes, R. M. Hill, J. Leggett, N. Rhodes, and R. Bowtell, *Theoretical Advantages of a Triaxial Optically Pumped Magnetometer Magnetoencephalography System*, NeuroImage **236**, 118025 (2021).

[26] R. J. Clancy, V. Gerginov, O. Alem, S. Becker, and S. Knappe, *A Study of Scalar Optically-Pumped Magnetometers for Use in Magnetoencephalography without Shielding*, ArXiv210502316 Phys. (2021).

[27] S. J. Seltzer and M. V. Romalis, *Unshielded Three-Axis Vector Operation of a Spin-Exchange-Relaxation-Free Atomic Magnetometer*, Appl. Phys. Lett. **85**, 4804 (2004).

[28] F. Beato, E. Belorizky, E. Labyt, M. Le Prado, and A. Palacios-Laloy, *Theory of a He 4 Parametric-Resonance Magnetometer Based on Atomic Alignment*, Phys. Rev. A **98**, (2018).

[29] J. Dupont-Roc, *Étude théorique de diverses résonances observables en champ nul sur des atomes « habillés » par des photons de radiofréquence*, J. Phys. **32**, 135 (1971).

[30] J. Dupont-Roc, *Détermination Par Des Méthodes Optiques Des Trois Composantes d'un Champ Magnétique Très Faible*, Rev. Phys. Appl. **5**, 853 (1970).

[31] A. Cerman and P. Ripka, *Towards Fully Digital Magnetometer*, Sens. Actuators Phys. **106**, 34 (2003).

[32] S. Belyayev and N. Ivchenko, *Digital Fluxgate Magnetometer: Design Notes*, Meas. Sci. Technol. **26**, 125901 (2015).

[33] A. Cerman, A. Kuna, P. Ripka, and J. M. G. Merayo, *Digitalization of Highly Precise Fluxgate Magnetometers*, Sens. Actuators Phys. **121**, 421 (2005).